Selective Gas Phase Hydrogenation of

p-Chloronitrobenzene over Pd Catalysts:

Role of the Support

Fernando Cárdenas-Lizana[a], Yufen Hao[b], Micaela Crespo-Quesada[a], Igor Yuranov[a],

Xiaodong Wang[b], Mark A. Keane[b] and Lioubov Kiwi-Minsker[a*]*

[a]Group of Catalytic Reaction Engineering, Ecole Polytechnique Fédérale de Lausanne

(GGRC-ISIC-EPFL), Lausanne CH-1015, Switzerland

[b]Chemical Engineering, School of Engineering and Physical Sciences,

Heriot-Watt University, Edinburgh EH14 4AS, Scotland

*corresponding authors:

tel.: +44(0)131 451 4719, e-mail: M.A.Keane@hw.ac.uk

tel.: +41(0) 21 693 3186, e-mail: Lioubov.kiwi-minsker@epfl.ch

Abstract

The gas phase (1 atm, 453 K) hydrogenation of p-chloronitrobenzene (p-CNB) over a series of laboratory synthesised and commercial (activated carbon (AC), *non*-reducible (SiO_2 and Al_2O_3) and reducible (ZnO) oxide) supported Pd (1-10 % wt.) has been examined. Laboratory synthesis involved standard impregnation and deposition of monodispersed *nano*-scale Pd^0 particles. Reaction over these catalysts generated the target p-chloroaniline (p-CAN) (*via* selective hydrogenation) and nitrobenzene (NB)/aniline (AN) as a result of a combined hydrodechlorination/hydrogenation. A range of mean Pd particle sizes (2.4-12.6 nm) exhibiting different electronic character (from XPS analysis) was generated. Particle size was determined by electron microscopy and (H_2 and CO) chemisorption. p-CNB consumption rate and H_2 chemisorption both increased with decreasing Pd particle size. The presence of residual Mo from the $Na_2MoO_4 \cdot H_2O$ stabilizer in catalyst synthesis by colloidal deposition suppressed activity but this was circumvented by the use of poly N-vinyl-2-pyrrolidone (PVP) as stabilizer. Pd/AC generated p-CAN and AN as principal products, Pd on SiO_2 and Al_2O_3 exhibited hydrodechlorination character (generating AN and NB) while Pd/ZnO promoted the sole formation of p-CAN at all levels of conversion. Reaction selectivity is linked to Pd site electron density where the formation of $Pd^{\delta+}$ (on AC) activates the nitro group with subsequent C-Cl bond scission and the occurrence of $Pd^{\delta-}$ (on SiO_2 and Al_2O_3) favours interaction *via* the aromatic ring that activates both $-NO_2$ and $-Cl$ for attack. Reaction exclusivity to p-CAN over Pd/ZnO is attributed to the formation of supported PdZn (demonstrated by XPS), which selectively activates the $-NO_2$ group. This is the first report that demonstrates 100% selectivity for p-CNB $\rightarrow p$-CAN over supported Pd.

Keywords: Supported Pd; p-chloronitrobenzene hydrogenation; p-chloroaniline; PdZn alloy; support effects.

1. Introduction

Functionalised anilines are key intermediates in the synthesis of fine chemicals, herbicides, pesticides, dyes and pigments (1). Amine production *via* nitroarene hydrogenation has been promoted using a range of (carbon (2-5), Al_2O_3 (6-10), SiO_2 (11-13), TiO_2 (14-17), CeO_2 (18), Fe_2O_3 (18-20), Fe_3O_4 (19), SnO_2 (21), CeO_2 (18,22) and polymer (23)) supported metal (Pd (2-7,16,24), Pt (11,20,23,25,26), Ru (21,26-28), Rh (29), Ni (8,10,14,30), Cu (31), Ag (13,32) and Au (33,34)) catalysts. Taking the hydrogenation of *p*-chloronitrobenzene (*p*-CNB), undesired C-Cl scission (Scheme 1) is difficult to circumvent, particularly at high conversions (33,35). To date, *p*-CNB hydrogenation has focused on liquid phase batch reactions at high H_2 pressure (up to 60 atm) (30). A move from batch to continuous operation has been identified (36) as a priority for sustainable production in the pharmaceutical and fine chemical sectors. We have demonstrated (34) exclusive $-NO_2$ reduction (but at low reaction rate) in the continuous gas phase hydrogenation of substituted nitroarenes over supported Au. In examining the role of Pd as promoter to increase activity, selective *p*-chloroaniline (*p*-CAN) production was achieved for Au/Pd $\geq$ 20 (9). Increasing the Pd content delivered higher rates but with the formation of nitrobenzene (NB). This is consistent with the literature on gas (16) and liquid (7,35) phase operation that has demonstrated non-selective CNB hydrogenation over supported Pd, generating aniline (AN) (7,16,35), NB (7,16,35) and azo-compounds (16) as by-products.

Catalytic activity/selectivity in nitro-group reduction can be governed by the electronic (18,22) and crystallographic (15) character of the metal phase that is, in turn, influenced by

3

interactions with the carrier (12,37). Support acid-base properties can impact on metal dispersion with electron transfer resulting in the formation of partially charged *nano*-scale particles (38,39). Sangeetha *et al.* (40) observed higher activity in the hydrogenation of NB over Pd/hydrotalcite relative to Pd/MgO and Pd/γ-Al$_2$O$_3$, which they linked to enhanced Pd dispersion due to support basicity. Higher CAN selectivity (from CNB) has also been achieved with the incorporation of metal cations (Cr^{3+}/Cr^{2+} (41) and Sn^{4+} (7)) on supported Pd and associated with enhanced polarization of the N=O bond (7). When reducible oxides are used as carriers, partial reduction of the support can lead to alloy formation (42). Recent work has demonstrated selective hydrogenation of functionalized alkynes over PdZn alloy (43,44). The formation of a PdZn phase, established by high-resolution x-ray diffraction/absorption spectroscopy, has been shown to enhance selectivity in the hydrogenation of 1-pentyne to pentenes (relative to Pd/SiO$_2$) (45) and acetonitrile to ethylamine (compared with Pd black) (46). Use of supported Pd catalysts to achieve high selectivity in the conversion of *p*-CNB to *p*-CAN represents a challenge. We have set out to identify the critical variable(s) that control –NO$_2$ group reduction selectivity by examining a range of (commercial and laboratory synthesised) catalysts with varying Pd content, support and method of preparation. We compare the catalytic action of bulk (unsupported) Pd with that of Pd supported on three distinct carriers; (i) activated carbon; (ii) *non*-reducible oxides (SiO$_2$ and Al$_2$O$_3$); (iii) ZnO.

2. Experimental

2.1. Catalyst Preparation and Activation

The activated carbon support (AC, 905 m^2 g^{-1}) was obtained from NORIT (UK) and subjected to a demineralization treatment (1 M HNO_3 under continuous stirring at 500 rpm for 7 days) to remove any residual metal that could contribute to the hydrogenation process. The AC support was thoroughly washed with deionized water (until pH of the wash water approached 7) and oven-dried at 383 K for 12 h. The oxide supports, SiO_2 (Cab-O-Sil M-5, Cabot), Al_2O_3 (Puralox, Condea Vista Co.) and ZnO (Aldrich) were used as received. A series of (AC, SiO_2 and Al_2O_3) supported Pd catalyst precursors were prepared by standard impregnation (with $Pd(NO_3)_2$ at 363 K) and denoted as Pd/AC-I, Pd/SiO_2 and Pd/Al_2O_3-III. The impregnated samples were oven dried at 393 K for 12 h. In addition, Pd/Al_2O_3-I, Pd/ZnO and Pd/ZnO-PVP were prepared by deposition of *ex-situ* synthesized monodispersed Pd^0 nanoparticles. In the case of Pd/Al_2O_3-I and Pd/ZnO, an aqueous solution of $PdCl_2$ (Fluka, >99 %) and $Na_2MoO_4·H_2O$ (Fluka, >99 %) (Pd/Mo mol ratio = 1) was heated at 368 K (under continuous stirring, 500 rpm) until complete evaporation. The solid residue was dissolved in water and contacted (at ambient temperature) with a continuous flow of H_2 (100 cm^3 min^{-1}) for 30 min. This procedure has been demonstrated (47) to result in the formation of uniform Pd^0 nanoparticles stabilised by molybdate anions. The *ex-situ* synthesis of monodispersed PVP (poly N-vinyl-2-pyrrolidone, Aldrich) stabilised Pd nanoparticles followed the method described by Lim *et al.* (48). A known mass (0.277 g) of PVP and ascorbic acid (0.156 g, 99%, Aldrich), which acts as reducing agent, were dissolved in 15 cm^3 water at 368-371 K. An aqueous solution of $PdCl_2$ (0.088 g, 60% Pd, Aldrich) and NaCl (0.058 g, 99.5%, Fluka)

was added under constant agitation (*ca.* 500 rpm) with an instantaneous change in color (from brown to black), indicative of Pd reduction and colloid formation (48). The colloidal solution was kept under agitation at 368-371 K) for 3 h, cooled and diluted with 75 cm^3 acetone and left for 12 h. The colorless liquid was decanted and the black viscous residue dissolved to give an homogeneous and stable Pd(PVP) colloidal solution. Palladium deposition (on ZnO) was achieved *via* adsorption where the support (*ca.* 2 g) was immersed and stirred in the Pd colloidal solution for *ca.* 2 h, the slurry filtered and dried in air at ambient temperature. Two commercial supported catalysts (Pd/AC-II and Pd/Al$_2$O$_3$-II, Aldrich) and bulk PdO (Aldrich) were also examined. Prior to use, the catalysts were sieved into a batch of 75 μm average diameter and reduced in 60 cm^3 min^{-1} H$_2$ at 10 K min^{-1} to 573 K, which was maintained for 1 h. Samples for off-line analysis were passivated in 1% v/v O$_2$/He at ambient temperature.

2.2. Catalyst Characterisation

The Pd content was measured by inductively coupled plasma-optical emission spectrometry (ICP-OES, Vista-PRO, Varian Inc.) from the diluted extract in HF. Temperature programmed reduction (TPR), H$_2$ and CO chemisorption and BET surface area were determined using the commercial CHEM-BET 3000 (Quantachrome) unit. The samples were loaded into a U-shaped Quartz cell (3.76 mm i.d.) and heated in 17 cm^3 min^{-1} (Brooks mass flow controlled) 5% v/v H$_2$/N$_2$ at 10 K min^{-1} to 573±1 K. The effluent gas passed through a liquid N$_2$ trap and H$_2$ consumption monitored by a thermal conductivity detector (TCD) with data acquisition/manipulation using the TPR Win^{TM} software. The reduced samples were maintained at 573 K until the signal returned to baseline, swept with 65 cm^3 min^{-1} N$_2$ for 1.5

h, cooled to ambient temperature and subjected to H_2 (or CO) chemisorption using a pulse (10 μl) titration procedure. In a series of blank tests, chemisorption measurements on each support (AC, Al_2O_3, SiO_2 and ZnO) did not result in any detectable uptake. BET areas were recorded with a 30% v/v N_2/He flow using pure N_2 (99.9%) as internal standard. At least two cycles of N_2 adsorption-desorption in the flow mode were employed to determine total surface area using the standard single point method. BET surface area, H_2 and CO uptake were reproducible to within ±5 %; the values quoted represent the mean.

X-ray photoelectron spectroscopy (XPS) analyses were conducted on an Axis Ultra instrument (Kratos Analytical) under ultra-high vacuum conditions ($<10^{-8}$ Torr) using a monochromatic Al Kα X-ray source (1486.6 eV). The source power was maintained at 150 W and the emitted photoelectrons were sampled from a 750×350 μm^2 area at a take-off angle = 90°. The analyser pass energy was 80 eV for survey spectra (0–1000 eV) and 40 eV for high resolution spectra (Pd $3d_{5/2}$ and Pd $3d_{3/2}$). The adventitious carbon 1s peak was calibrated at 284.5 eV and used as an internal standard to compensate for any charging effects. Spectra curve fitting and quantification were performed with the Casa XPS software, using relative sensitivity factors provided by Kratos. Palladium particle morphology and size were determined by transmission electron microscopy analysis; JEOL JEM 2011 HRTEM unit with a UTW energy dispersive X-ray detector (Oxford Instruments) operated at an accelerating voltage of 200 kV using Gatan Digital Micrograph 3.4 for data acquisition/manipulation. The samples for analysis were crushed and deposited (dry) on a holey carbon/Cu grid (300 Mesh). Mean Pd size was based on a count of up to 800 individual Pd particles.

2.3. Hydrogenation of p-Chloronitrobenzene (p-CNB)

2.3.1. Catalytic System

The hydrogenation of p-CNB (Sigma-Aldrich, purity ≥99 %) as a solution in ethanol (Sigma-Aldrich, ≥99 %) was carried out *in situ*, immediately after catalyst activation, under atmospheric pressure at 453 K in a fixed bed vertical glass reactor (*i.d.* = 15 mm). The operating conditions ensured negligible heat/mass transport constraints. A layer of borosilicate glass beads served as preheating zone where the p-CNB reactant was vaporized and reached reaction temperature before contacting the catalyst. Isothermal conditions (±1 K) were ensured by diluting the catalyst bed with ground glass (75 μm). The reaction temperature was continuously monitored using a thermocouple inserted in a thermowell within the catalyst bed. p-CNB was delivered at a fixed calibrated flow rate to the reactor *via* a glass/teflon air-tight syringe and teflon line using a microprocessor controlled infusion pump (Model 100 kd Scientific). A *co*-current flow of p-CNB and ultra pure (BOC, >99.99 %) H_2 (<1 % v/v p-CNB in H_2) was maintained at $GHSV = 2\times10^4$ h^{-1} with an inlet flow (F) over the range $24\times10^{-4} - 7\times10^{-4}$ mol h^{-1}. The H_2 content was up to 110 times in excess of the stoichiometric requirement for hydrogenation to p-CAN and the flow rate was monitored using a Humonics (Model 520) digital flowmeter. The molar Pd (n) to F ratio spanned the range $1\times10^{-3} - 9\times10^{-3}$ h. In a series of blank tests, passage of p-CNB in a stream of H_2 through the empty reactor or over the support alone did not result in any detectable conversion. The reactor effluent was frozen in a liquid nitrogen trap for subsequent analysis.

2.3.2. Analytical Method and Activity/Selectivity Measurements

The composition of the reactant/product(s) mixtures was determined using a Perkin-Elmer Auto System XL chromatograph equipped with a programmed split/splitless injector and a flame ionization detector, employing a DB-1 capillary column (*i.d.* = 0.33 mm, length = 30 m, film thickness = 0.20 μm). Data acquisition and manipulation were performed using the TotalChrom Workstation Version 6.1.2 (for Windows) chromatography data system and the overall reactant/product molar fractions (x_i) were determined from detailed calibration plots (not shown). Fractional hydrogenation ($X_{p\text{-}CNB}$) was obtained from

$$X_{p-CNB} = \frac{[p-CNB]_{in} - [p-CNB]_{out}}{[p-CNB]_{in}}$$

where selectivity with respect to *p*-CAN is given by

$$S_{p-CAN}(\%) = \frac{[p-CAN]_{out}}{[p-CNB]_{in} - [p-CNB]_{out}} \times 100$$

Repeated reactions with different samples from the same batch of catalyst delivered conversion/selectivity values that were reproducible to within ± 7 %.

3. Results and Discussion

3.1. Catalyst Characterisation

Characterisation measurements for the series of Pd catalysts studied are presented in Tables 1 and 2. Commercial and laboratory synthesized samples exhibiting a range of Pd loading (0.9-10.2 % w/w) and BET area (2-875 m^2 g^{-1}) have been used in this work to promote *p*-CNB hydrogenation. We must stress that a very broad set of Pd catalysts were chosen in order to establish critical characteristics that determine activity and selectivity.

3.1.1. Palladium Particle Size

Representative temperature programmed reduction (TPR) profiles (for PdO, Pd/AC-II, Pd/Al$_2$O$_3$-II and Pd/ZnO) are presented in Figure 1. Each profile is characterised by the appearance of a negative peak at 343-377 K (Table 2) that can be attributed to Pd hydride decomposition. Ambient temperature H$_2$ absorption is known to generate β-phase Pd hydride when the H$_2$ partial pressure exceeds 0.02 atm (49,50); P_{H2} during TPR in this work = 0.05 atm. The hydride is thermally unstable and decomposes during thermal treatment to release H$_2$ over the temperature range 342-386 K (51-53). Hydride composition, presented in Table 2 as a H/Pd ratio, is known to depend on Pd particle size (10,54) where H/Pd decreases with decreasing size (increasing metal dispersion) (51) to approach zero for Pd size <2.5 nm (51,55). Bulk Pd, as our benchmark, is characterized by the highest H/Pd (0.67), a result in good agreement with values (0.66-0.73) reported in the literature (54,56). Considering the supported catalysts, the commercial Pd/Al$_2$O$_3$-II exhibited the lowest H/Pd (0.05) while the remaining systems generated ratios in the range 0.16-0.36, characteristic of Pd particles of 3-24 nm (56,57). The positive signal at higher temperature (T_{max} = 573 K) for Pd/ZnO (Figure 1 (IV)) has been observed previously and linked to: (i) secondary reduction of an oxidised Pd component or reduction of ZnO (or ZnCl$_2$) at the metal/support interface (58); (ii) simultaneous reduction of Pd^{2+} and Zn^{2+} resulting in the formation of PdZn particles (59).

The (mean) Pd particle sizes determined from TEM and (CO and H$_2$) chemisorption are given in Table 2. Consistent values for all three measurements were obtained in the case of Pd/Al$_2$O$_3$-II (2.2±0.2 nm), which agree with the low associated H/Pd from TPR analysis.

However, there are inconsistencies in the results generated with each technique for the other supported Pd samples. We should note that there is a dearth of published studies recording Pd particle sizes using more than one analytical methodology. Taking an overview of the published work on supported metals in general, both agreement (4,51,60-62) and disagreement (52,62-64) have resulted from the estimation of metal particle size using gas chemisorption and TEM analysis. The discrepancy can be linked to limitations associated with these techniques. In the case of chemisorption, a source of error can result from a partial (or total) active phase occlusion by residual precursor species *post*-activation that serve to suppress uptake, leading to an *over*-estimation of metal particle size (63,64). CO chemisorption delivered a range of Pd sizes that do not correlate directly with Pd hydride composition and deviate significantly from values obtained from H_2 uptake and TEM. This may be the result of applying a fixed Pd/CO adsorption stoichiometry (52,65) (surface metal atoms/CO molecules chemisorbed = 2), as has been the standard approach for carbon and oxide supported Pd systems (66,67). However, CO can adsorb on Pd in both linear (Pd:CO = 1:1) (68) and bridged (Pd:CO = 2:1) (68,69) forms and this appears to depend on the nature of the support (70) and Pd size (71). Hydrogen chemisorption is commonly employed to estimate Pd dispersion (63,72) where a dissociative adsorption (Pd:H stoichiometry = 1:1) is applied. Prelazzi *et al.* (73), in reviewing the available literature, have identified instances of good agreement between H_2 uptake (taking Pd:H = 1:1) and TEM data. In this study, Pd sizes obtained from H_2 chemisorption differ from the TEM derived values but both methods delivered an equivalent trend in terms of increasing (or decreasing) size across the group of

catalysts. Particle size measurements from H_2 chemisorption can be compromised due to hydrogen spillover, *i.e.* dissociative chemisorption on metal sites with transport to the support surface (74), which results in an apparent higher Pd dispersion (*under*-estimation of metal size) due to additional H_2 consumption. Indeed, there is evidence in the literature for hydrogen spillover under ambient conditions for carbon (75) and oxide (76) supported Pd. We should flag Pd/AC-I that exhibits an unfeasibly large Pd size (129.0 nm) based on H_2 chemisorption. This can result from occlusion of Pd surface sites by amorphous carbon associated with the support, as noted elsewhere (64), leading to inhibited H_2 uptake.

Electron microscopy as an imaging technique provides a particle size distribution from which the mean can be determined. There are certain limitations in the application of this method, as highlighted in the review of Matyi *et al.* (65) and recently published analysis by Liu (77). This approach provides a two dimensional imaging of three dimensional nanoparticulate structures where the occurrence of irregular morphologies, as a result of metal-support interactions, presents problems in terms of consistent diameter measurement. Accurate diameter estimation can also be compromised by poor contrast between the support and metal(s) phases while apparatus detection limit (sizes below 1-2 nm (78)) can also lead to inaccurate sizes. Representative TEM micrographs and associated Pd particle size distributions on carbonaceous, reducible and *non*-reducible oxide carriers are presented in Figure 2. The supported metal phase exhibits a *pseudo*-spherical morphology with particles predominantly <10 nm. It is critical in TEM analysis that the particle population used for size estimation is representative of the entire ensemble of crystallites. Taking Pd/C-II as an

example, the standard deviation of the mean (σ_m) is presented as a function of Pd particle count (inset to Figure 2 (I)), following the approach reported previously (78). It can be seen that σ_m is sensitive to the total number of Pd particles counted and σ_m invariance (at counts >200) ensures that the size distribution is truly representative. Invariance of the mean applies to all the d_{TEM} values recorded in Table 2. While the combination of techniques used in this study should be complementary, our results suggest that the chemisorption measurements (particularly CO) do not give a reliable measure of Pd size. TEM analysis delivers the more valid Pd size information where particle counting is conducted with statistical rigour. Hydrogen uptake capacity is, nonetheless, an important consideration in H_2 mediated catalysis. The correlation between H_2 uptake (at ambient temperature) and mean Pd size (from TEM) is presented in Figure 3 (I), where there is a clear increase in H_2 chemisorption capacity with decreasing Pd NP size (12.6→2.4 nm). This tendency is in agreement with published literature (51,57) showing enhanced H_2 chemisorption for smaller Pd particles.

3.1.2. Palladium Electronic Characteristics

In order to gain insight into the electronic character of the Pd phase, XPS analysis over the Pd $3d$ binding energy (BE) region was conducted with peak deconvolution, as shown in Figure 4 for Pd/ZnO. It is known that the support can impact on the electronic properties of the metallic phase *via* metal-support interactions (79), which are more pronounced for Pd particles at the nano-scale. Taking bulk Pd as benchmark, the core level Pd $3d_{5/2}$ BE (= 335.3 eV) is in good agreement with the value (335.2 ± 0.2 eV) reported by Briggs and Seah (80) for Pd^0. In order to explicitly probe modification(s) to Pd electron density due to particle size,

we present the relationship between d_{TEM} and Pd $3d_{5/2}$ BE in Figure 5. The BE values exhibited a measurable increase (334.7→334.9 eV) with decreasing mean Pd size (6.4→2.4 nm) for the Al_2O_3 system, as has been noted elsewhere (81). Moreover, the BE showed a marked dependence on the support. Palladium on AC exhibits a Pd $3d_{5/2}$ BE that is *ca.* 0.6 eV higher than bulk Pd, suggesting electron transfer from Pd to the carbon support resulting in a partial positively charged metal phase ($Pd^{\delta+}$). Jiang and co-workers (82) observed a positive displacement (*ca.* 1.1 eV) for carbon supported Pd (3-12 nm) when compared with bulk Pd that they ascribed to metal-support interactions. Ramos *et al.* (83) reported a shift to higher BE for Pd/C that was attributed to electronic transfer associated with residual surface Cl. Gómez-Sainero *et al.* (84) have also demonstrated the occurrence of electron-deficient Pd (3.8-10.5 nm) on a carbon carrier. They linked this to the presence of surface species (*e.g.* HCl and NO_x) generated during catalyst preparation/activation that serve to modify the electron density of the Pd sites with the formation of supported Pd^{n+}. The presence of $Pd^{\delta-}$ on Al_2O_3 and SiO_2 follows from the observed lower (by 0.4-0.6 eV) BE (relative to bulk Pd), as shown in Figure 5. Oxidic supports have been found to influence the electronic properties of supported transition metals where a change in the electron density of Ru (2-10 nm) on MgO, Al_2O_3 and SiO_2 has been attributed to interaction with surface OH groups (85). The Pd $3d_{5/2}$ spectrum for Pd/ZnO (Figure 4) suggests the presence of two distinct surface Pd species. The main component shows a BE (335.0 eV) close to the reference for zero valent Pd (80) while a secondary component exhibits a signal shifted to higher BE (by 0.7 eV) and can be attributed to the occurrence of PdZn (58). The formation of an intermetallic PdZn alloy phase after H_2

treatment at $T \geq 373$ K has been demonstrated by HRXRD and XAS (45) but the mechanism is still a matter of some debate. Hong *et al.* (76) have proposed the growth of a thin PdZn alloy phase at the metal-support interface resulting in a strong anchoring of the metal that serves to inhibit sintering. Alternatively, reversible migration and transformation of ZnO (to Zn) on Pd can result in the partial/total coverage of Pd clusters and the ultimate formation of a PdZn outerlayer (58).

3.2. Correlation of Catalyst Characteristics with Catalytic Performance

3.2.1. Activity

The catalytic response of supported metal nanoparticles in hydrogenation reactions can be governed by electronic (86) and/or geometric (87,88) considerations. A series of experiments were conducted to investigate the effect of particle size on catalyst performance where an increase in activity with decreasing Pd size (12.6→2.4 nm) is apparent from the entries in Figure 3 (II). The results suggest that the nature of the carrier (carbon *vs.* oxide) or catalyst source (laboratory synthesized or commercial) does not impact significantly on rate, which is determined by Pd size. Indeed, similar activity was obtained for catalysts with an equivalent mean Pd size on different supports (Pd/AC-I (11.7 nm) and Pd/SiO$_2$ (12.6 nm)) while, taking a common support (Pd/AC-I (11.7 nm) and Pd/AC-II (4.4 nm)), a four-fold higher activity was recorded for the catalyst bearing smaller Pd particles. This response has also been observed for gas phase *p*-CNB hydrogenation over supported Au (22) but we provide here the first report of Pd size effects in this reaction. We should note that the opposite trend has been reported for batch liquid phase *p*-CNB hydrogenation where higher

activities were recorded for Pt/Al$_2$O$_3$ with lower metal dispersion and ascribed to stabilization of the negatively charged reaction transition state on larger Pt particles (89). A salient feature of the data generated in this study is the match of activity dependence on Pd size with that of H$_2$ chemisorption (Figure 3 (I)). Increased rate can be attributed to greater surface hydrogen, which is a feature of greater Pd dispersion. We should flag Pd/Al$_2$O$_3$-I and Pd/ZnO, synthesized by deposition of (Na$_2$MoO$_4$·H$_2$O) stabilized monodispersed Pd nanoparticles prepared *ex situ*, that deviate from the general trend in delivering lower activities. This can result from residual surface stabilizer *post*-activation that occludes active sites and inhibits rate, as has been reported for the hydrogenation of acetylene (90). Indeed, XPS analysis has established the presence of surface Mo species (≤1% w/w) in activated Pd/Al$_2$O$_3$-I and Pd/ZnO that is consistent with an earlier report of a Pd nanoparticulate catalyst prepared using Na$_2$MoO$_4$·H$_2$O as stabilizer (43). Zina and Ghorbel (91) have demonstrated that inclusion of Mo in zeolite supported Pd suppressed 1,3-butadiene hydrogenation activity, which was linked to the formation of Pd$_n$Mo$_m$ clusters. It should, however, be noted that H$_2$ chemisorption on Pd/Al$_2$O$_3$-I and Pd/ZnO was consistent with the general trend line shown in Figure 3 (I). This suggests that any Mo remaining from the stabilizer does not impact on H$_2$ uptake but must influence *p*-CNB adsorption/activation.

3.2.2. Selectivity

The main reaction pathways in the hydrogenation of *p*-CNB are identified in Scheme 1 where nitro group reduction (step I) generates the target amine (*p*-CAN). Dechlorination of *p*-CNB (step II) results in the formation of nitrobenzene (NB), which can undergo further

hydrogenation (step III) or dechlorination of p-CAN (step IV) to give, in both cases, aniline (AN). Reaction over the Pd catalysts in this study generated p-CAN, NB and/or AN in varying proportions. In such a parallel/sequential reaction mechanism, selectivity is only meaningful at an equivalent level of conversion (X_{p-CNB}), which we set at 0.2 in Table 1. Bulk Pd was employed as benchmark, serving as an index against which Pd particle size and Pd-support effects can be evaluated. Reaction over unsupported Pd generated all three products with the principal formation of AN (composite hydrodechlorination and hydrogenation). Taking an overview of the catalytic response exhibited by the supported catalysts, three groups emerge, *i.e.* Pd on carbon, *non*-reducible oxides and ZnO, which are separated by the dashed lines in Tables 1 and 2. Carbon supported Pd (Pd/AC) promoted hydrogenation and hydrodechlorination steps with p-CAN selectivity that deviated from that observed for bulk Pd. Palladium on *non*-reducible Al_2O_3 and SiO_2 did not generate any detectable p-CAN but exhibited hydrodechlorination character (to produce NB and AN). In marked contrast, Pd/ZnO was 100% selective to p-CAN. The latter is a very significant finding as, to the best of our knowledge, there have been no reports demonstrating reaction exclusivity to p-CAN in the gas phase hydrogenation of p-CNB over supported Pd. Given the distinct selectivity response for the three groupings, one catalyst (commercial Pd/AC-II and Pd/Al_2O_3-II and laboratory synthesised Pd/ZnO) was chosen from each group for further comprehensive catalyst testing; the relationships between conversion (X_{p-CNB}) and selectivity (S_i) are shown in Figure 6. At low X_{p-CNB} (<0.05), p-CAN was the principal product over bulk Pd (Figure 6 (I)) with the preferential formation of AN at higher conversions and NB as a secondary product.

This suggests Pd activation of both $-NO_2$ and $-Cl$ functionalities and is in agreement with published literature showing that dechlorination (92) and nitro-group reduction (41) are promoted over unsupported Pd. The switch in selectivity to C–Cl bond scission and AN formation can be linked to the electron-donating character of the $-NH_2$ function (relative to electron-withdrawing $-Cl$ and $-NO_2$), which can induce electron transfer *via* the benzene ring, increasing C−Cl polarity (93,94) and facilitating hydrogenolytic attack by dissociated H. In the case of Pd/AC-II (Figure 6 (II)), *p*-CAN and AN were the principal products with trace formation of NB. XPS measurements are consistent with the formation of $Pd^{\delta+}$ in Pd/AC. The nitro group exhibits a higher relative electronegativity than the *para*-substitued Cl where the ring inductive and conjugative effects serve to increase the electron density of $-NO_2$ (93) with activation at electron-deficient Pd to generate *p*-CAN formation, as reported elsewhere (95,96). In common with bulk Pd, a decrease in selectivity to *p*-CAN with increased AN is in evidence at higher X_{p-CNB} (>0.3), indicating a sequential mechanism *via* steps (I) and (IV) (Scheme 1). Functionalised chlorobenzenes can interact with $Pd^{\delta+}$ through the Cl substituent with a weakening of the C-Cl (97), facilitating hydrogenolysis to AN. In contrast, NB and AN were the only products generated over Pd/Al$_2$O$_3$-II (Figure 6 (III)), where an increase in conversion (>0.3) was accompanied by higher AN selectivity, suggesting that dechlorination preceded NB hydrogenation, *i.e.* reaction *via* steps (II) and (III) in Scheme 1. Both $-NO_2$ and $-Cl$ functions can reduce the electron density of the benzene ring, favouring interaction with $Pd^{\delta-}$ in Pd/Al$_2$O$_3$-II, where both substituents are activated. The ring carbon bonded to Cl is

more susceptible to hydrogenolytic attack as it bears the lowest electron density of all the carbons in the ring (93), leading to NB formation with further hydrogenation to AN.

Reaction over Pd/ZnO (Figure 6 (IV)) generated p-CAN as the sole product, regardless of conversion, *i.e.* exclusive reaction *via* path (I) in Scheme 1. The Pd/ZnO catalyst is characterized by a Pd $3d_{5/2}$ core level BE close to that of the reference Pd (Figure 5). As both hydrodechlorination and hydrogenation were promoted over bulk Pd, a similar product distribution should be expected for Pd/ZnO. However, the formation of PdZn alloy, demonstrated by XPS (Figure 4), must influence p-CNB adsorption and surface reaction. Sárkány *et al.* (58) reported the complete suppression of butane formation in the hydrogenation of 1,3-butadiene due to the formation of a PdZn intermetallic phase and attributed this to weaker diene/surface interaction. Iwasa *et al.* (46) recorded enhanced selectivity to primary amine in acetonitrile hydrogenation over Pd/ZnO, ascribing this to differences in substrate and/or intermediate adsorption strength relative to other supported Pd catalysts. XPS analysis has established the formation of zero valent Pd with a lesser (34 % w/w) PdZn component. We envisage H_2 dissociation on Pd^0 to generate surface reactive hydrogen where p-CNB interaction with the PdZn phase selectively activates the $-NO_2$ function. Indeed, reaction of p-CAN over Pd/ZnO delivered AN as the sole product where the rate (1.6 mol$_{p\text{-CAN}}$ h^{-1} mol$_{Pd}^{-1}$) was appreciable lower than that (13.5 mol$_{p\text{-CAN}}$ h^{-1} mol$_{Pd}^{-1}$) recorded for p-CNB as reactant. This is consistent with exclusivity to p-CAN where path (IV) (in Scheme 1) does not contribute to the overall process for Pd/ZnO.

3.2.3. Role of the Stabilizer in Determining Pd/ZnO Performance

In order to establish the possible effect of the stabilizer on the catalytic response exhibited by the catalysts synthesised using the colloid route with $Na_2MoO_4 \cdot H_2O$, an additional ZnO supported Pd was prepared, employing PVP as stabilizer (see Experimental section), which we label Pd/ZnO-PVP. The as-prepared sample was calcined at 873 K as there is evidence in the literature for the removal of capping polymers at $T \geq 550$ K (98). There was no detectable (on the basis of XPS analysis, not shown) surface nitrogen associated with the calcined sample, indicating effective PVP removal. Subsequent TPR activation, following the same procedure applied to Pd/ZnO (see Experimental section), generated an equivalent XPS response (profile not shown) with a principal Pd^0 (BE = 335.0 eV) and secondary PdZn (31% w/w, BE = 335.7 eV) component. Palladium particle size distribution from TEM analysis delivered a larger mean Pd size (11.4 nm) for Pd/ZnO-PVP relative to Pd/ZnO (6.5 nm) that can be attributed to sintering during the calcination step. Reaction of p-CNB over Pd/ZnO-PVP resulted in the sole formation of the target p-CAN. Reaction exclusivity in nitro-group reduction for both ZnO supported Pd catalysts can be explicitly attributed to the supported PdZn phase. Pd/ZnO-PVP delivered a greater hydrogenation rate than Pd/ZnO (Figure 3 (II)) although the former exhibited larger Pd particle size. This confirms rate inhibition by residual Mo in the case of Pd/ZnO. The correlation of H_2 chemisorption (Figure 3 (I)) and activity (Figure 3 (II)) with Pd size for Pd/ZnO-PVP coincides with the general trend. Our results demonstrate enhanced hydrogenation activity for smaller nano-scale Pd particles irrespective of support, rate suppression due to the presence of residual (Mo-containing) stabilizer and PdZn promotion of full selectivity to p-CAN.

4. Conclusions

We have established that the support (activated carbon (AC), *non*-reducible (SiO$_2$, Al$_2$O$_3$) and reducible (ZnO) oxides) can influence catalytic performance in Pd promoted gas phase hydrogenation of *p*-CNB. Characterisation of Pd particle size by TEM, H$_2$ and CO chemisorption has been assessed where the former is shown to give the most reliable results when particle counting is statistically robust. Chemisorption leads to erroneous values arising from (i) the application of an exclusive adsorption stoichiometry factor, (ii) possible Pd site occlusion and/or (iii) contribution due to spillover. Reaction rate and surface hydrogen both increase with decreasing mean Pd size (from 12.6 to 2.4 nm). A lower rate was recorded for particles prepared by a colloidal deposition technique, which is due to site blocking by residual Mo from the stabilizer (Na$_2$MoO$_4$·H$_2$O). Use of PVP as stabilizer (Pd/ZnO-PVP) circumvents Pd poisoning but the calcination step required to remove the polymer induces Pd agglomeration, which impacts on H$_2$ uptake and hydrogenation rate. Bulk Pd, used as a benchmark, promoted composite hydrodechlorination/hydrogenation to generate *p*-CAN, AN and NB. XPS analysis has demonstrated electron transfer from Pd to AC with the generation of Pd$^{\delta+}$ that activates both –Cl and –NO$_2$ functions with preferential *p*-CAN formation at low *p*-CNB conversion and increased selectivity to AN in subsequent dechlorination at higher conversions. Palladium supported on Al$_2$O$_3$ and SiO$_2$ was *non*-selective to *p*-CAN, exhibiting hydrodechlorination character with preferential NB formation at lower conversion and AN as major product at higher conversion. This can be accounted for in terms of repulsion between –NO$_2$ and –Cl and surface Pd$^{\delta-}$ leading to adsorption *via* the benzene ring, which facilitates

hydrogen attack of both substituents.   In complete contrast, Pd/ZnO (and Pd/ZnO-PVP) delivered *p*-CAN as the sole product, which is linked to the formation of a PdZn alloy that serves to activate the nitro function without further dechlorination.

Acknowledgments

References

(1)   Vogt, P. F.; Gerulis, J. J.   In *Ullmann's Encyclopedia of Industrial Chemistry. "Aromatic Amines",* Wiley-VCH: Weinheim, 2005; Vol. 1, p 2.

(2)   Bouchenafa-Saïb, N.; Grange, P.; Verhasselt, P.; Addoun, F.; Dubois, V., *Appl. Catal. A: Gen.* **2005**, 286, 167-174.

(3)   Kratky, V.; Kralik, M.; Mecarova, M.; Stolcova, M.; Zalibera, L.; Hronec, M., *Appl. Catal. A: Gen.* **2002**, 235, 225-231.

(4)   Neri, G.; Musolino, M. G.; Milone, C.; Pietropaolo, D.; Galvagno, S., *Appl. Catal. A: Gen.* **2001**, 208, 307-316.

(5)   Suh, D. J.; Park, T.-J.; Ihm, S.-K., *Ind. Eng. Chem. Res.* **1992**, 31, 1849-1856.

(6)   Vishwanathan, V.; Jayasri, V.; Basha, P. M., *React. Kinet. Catal. Lett.* **2007**, 91, 291-298.

(7)   Xu, Q.; Liu, X.-M.; Chen, J.-R.; Li, R.-X.; Li, X.-J., *J. Mol. Catal. A: Chem.* **2006**, 260, 299-305.

(8)   Meng, X.; Cheng, H.; Akiyama, Y.; Hao, Y.; Qiao, W.; Yu, Y.; Zhao, F.; Fujita, S.-I.; Arai, M., *J. Catal.* **2009**, 264, 1-10.

(9)   Cárdenas-Lizana, F.; Gómez-Quero, S.; Hugon, A.; Delannoy, L.; Louis, C.; Keane, M. A., *J. Catal.* **2009**, 262, 235-243.

(10)   Cárdenas-Lizana, F.; Gómez-Quero, S.; Keane, M. A., *Appl. Catal. A: Gen.* **2008**, 334, 199-206.

(11)   Takenaka, Y.; Kiyosu, T.; Choi, J.-C.; Sakakura, T.; Yasuda, H., *Green Chem.* **2009**, 11, 1385-1390.

(12)   Wang, X. D.; Liang, M. H.; Zhang, J. L.; Wang, Y., *Curr. Org. Chem.* **2007**, 11, 299-314.

(13)   Chen, Y.; Wang, C.; Liu, H.; Qiu, J.; Bao, X., *Chem. Commun.* **2005**, 42, 5298-5300.

(14)   Meng, X.-C.; Cheng, H.-Y.; Fujita, S.-I.; Hao, Y.-F.; Shang, Y.-J.; Yu, Y.-C.; Cai, S.-X.; Zhao, F.-Y.; Arai, M., *J. Catal.* **2010**, 269, 131-139.

(15)   Cárdenas-Lizana, F.; Gómez-Quero, S.; Idriss, H.; Keane, M. A., *J. Catal.* **2009**, 268, 223-234.

(16)   Sikhwivhilu, L. M.; Coville, N. J.; Pulimaddi, B. M.; Venkatreddy, J.; Vishwanathan, V., *Catal. Commun.* **2007**, 8, 1999-2006.

(17)   He, D. P.; Jiao, X. D.; Jiang, P.; Wang, J.; Xu, B. Q., *Green Chem.* **2012**, 14, 111-116.

(18)   Cárdenas-Lizana, F.; Gómez-Quero, S.; Perret, N.; Keane, M. A., *Catal. Sci. Technol.* **2011**, 1, 652-661.

(19)   Cárdenas-Lizana, F.; Gómez-Quero, S.; Kiwi-Minsker, L.; Keane, M. A., *Int. J. Nanotech.* **2012**, 9, 92-112.

(20)   Zhang, J.; Wang, Y.; Ji, H.; Wei, Y.; Wu, N.; Zuo, B.; Wang, Q., *J. Catal.* **2005**, 229, 114-118.

(21)   Zuo, B.; Wang, Y.; Wang, Q.; Zhang, J.; Wu, N.; Peng, L.; Gui, L.; Wang, X.; Wang, R.; Yu, D., *J. Catal.* **2004**, 222, 493-498.

(22)   Cárdenas-Lizana, F.; Gómez-Quero, S.; Perret, N.; Keane, M. A., *Gold Bull.* **2009**, 42, 124-132.

(23)   Xu, K.; Zhang, Y.; Chen, X.; Huang, L.; Zhang, R.; Huang, J., *Adv. Synth. Catal.* **2011**, 353, 1260-1264.

(24)   Figueras, F.; Coq, B., *J. Mol. Catal. A: Chem.* **2001**, 173, 223-230.

(25)   Zhao, F.; Ikushima, Y.; Arai, M., *J. Catal.* **2004**, 224, 479-483.

(26)   Liu, M.; Zhang, J.; Liu, J.; Yu, W. W., *J. Catal.* **2011**, 278, 1-7.

(27)   Liu, M.; Yu, W.; Liu, H., *J. Mol. Catal. A: Chem.* **1999**, 138, 295-303.

(28)   Tijani, A.; Coq, B.; Figuéras, F., *Appl. Catal.* **1991**, 76, 255-266.

(29)   Jang, Y.; Kim, S.; Jun, S. W.; Kim, B. H.; Hwang, S.; Song, I. K.; Kim, B. M.; Hyeon, T., *Chem. Commun.* **2011**, 47, 3601-3603.

(30)   Meng, X.; Cheng, H.; Fujita, S.-I.; Yu, Y.; Zhao, F.; Arai, M., *Green Chem.* **2011**, 13, 570-572.

(31)   Rao, K. N.; Reddy, B. M.; Park, S.-E., *Catal. Commun.* **2009**, 11, 142-145.

(32)   Cárdenas-Lizana, F.; Pedro, Z. Martínez de; Gómez-Quero, S.; Keane, M. A., *J. Mol. Catal.* **2010**, 326, 48-54.

(33)   Blaser, H. U.; Steiner, H.; Studer, M., *ChemCatChem* **2009**, 1, 210-221.

(34)   Cárdenas-Lizana, F.; Gómez-Quero, S.; Keane, M. A., *Catal. Commun.* **2008**, 9, 475-481.

(35)   Zou, J.-J.; Xiong, Z.; Wang, L.; Zhang, X.; Mi, Z., *J. Mol. Catal. A: Chem.* **2007**, 271, 209-215.

(36)   Jiménez-González, C.; Poechlauer, P.; Broxterman, Q. B.; Yang, B.-S.; Ende, D. A.; Baird, J.; Bertsch, C.; Hannah, R. E.; Dell'Orco, P.; Noorrnan, H.; Yee, S.; Reintjens, R.; Wells, A.; Massonneau, V.; Manley, J., *Org. Proc. Res. Dev.* **2011**, 15, 900-911.

(37)   Coq, B.; Figuéras, F., *Coord. Chem. Rev.* **1998**, 178-180, 1753-1783.

(38)   Stakheev, A. Y.; Mashkovskii, I. S.; Baeva, G. N.; Telegina, N. S., *Russ. J. Gen. Chem.* **2010**, 80, 618-629.

(39)   Stakheev, A. Y.; Sachtler, W. M. H., *J. Chem. Soc. Faraday Trans.* **1991**, 87, 3703-3708.

(40)   Sangeetha, P.; Shanthi, K.; Rao, K. S. R.; Viswanathan, B.; Selvam, P., *Appl. Catal. A: Gen.* **2009**, 353, 160-165.

(41)   Yang, X.; Liu, H.; Zhong, H., *J. Mol. Catal. A: Chem.* **1999**, 147, 55-62.

(42)   Cárdenas-Lizana, F.; Gómez-Quero, S.; Keane, M. A., *Catal. Lett.* **2009**, 127, 25-32.

(43)   Semagina, N.; Grasemann, M.; Xanthopoulos, N.; Renken, A.; Kiwi-Minsker, L., *J. Catal.* **2007**, 251, 213-222.

(44)   Crespo-Quesada, M.; Grasemann, M.; Semagina, N.; Renken, A.; Kiwi-Minsker, L., *Catal. Today* **2009**, 147, 247-254.

(45)   Tew, M. W.; Emerich, H.; van Bokhoven, J. A., *J. Phys. Chem. C* **2011**, 115, 8457-8465.

(46)   Iwasa, N.; Yoshikawa, M.; Arai, M., *Phys. Chem. Chem. Phys.* **2002**, 4, 5414-5420.

(47)   Maksimova, G. M.; Chuvilin, A. L.; Moroz, E. A.; Likholobov, V. A.; Matveev, K. I., *Kinet. Catal.* **2004**, 45, 870-878.

(48)   Lim, B.; Jiang, M. J.; Tao, J.; Camargo, P. H. C.; Zhu, Y.; Xia, Y., *Adv. Funct. Mater.* **2009**, 19, 189-200.

(49)   Shen, W. J.; Okumura, M.; Matsumura, Y.; Haruta, M., *Appl. Catal. A: Gen.* **2001**, 213, 225-232.

(50)   Shi, C.; Jang, B. W.-L., *Ind. Eng. Chem. Res.* **2006**, 45, 5879-5884.

(51)   Gómez-Quero, S.; Cárdenas-Lizana, F.; Keane, M. A., *Ind. Eng. Chem. Res.* **2008**, 47, 6841-6853.

(52)   Amorim, C.; Keane, M. A., *J. Chem. Technol. Biotechnol.* **2008**, 83, 662-672.

(53)   Mendez, C. M.; Olivero, H.; Damiani, D. E.; Volpe, M. A., *Appl. Catal. B: Environ.* **2008**, 84, 156-161.

(54)   Boudart, M.; Hwang, H. S., *J. Catal.* **1975**, 39, 44-52.

(55)   Ziemecki, S. B.; Michel, J. B.; Jones, G. A., *React. Sol.* **1986**, 2, 187-202.

(56)   Amorim, C.; Keane, M. A., *J. Colloid Interface Sci.* **2008**, 322, 196-208.

(57)   Jujjuri, S.; Keane, M. A., *Chem. Eng. J.* **2010**, 157, 121-130.

(58)   Sárkány, A.; Zsoldos, Z.; Furlong, B.; Hightower, J. W.; Guczi, L., *J. Catal.* **1993**, 141, 566-582.

(59)   Musolino, M. G.; Busacca, C.; Mauriello, F.; Pietropaolo, R., *Appl. Catal. A: Gen.* **2010**, 379, 77-86.

(60)   Bonarowska, M.; Burda, B.; Juszczyk, W.; Pielaszek, J.; Kowalczyk, Z.; Karpiński, Z., *Appl. Catal. B: Environ.* **2001**, 35, 13-20.

(61)   Bonivardi, A. L.; Baltanas, M. A., *J. Catal.* **1992**, 138, 500-517.

(62)   Benitez, J. L.; Angel, G. Del, *React. Kinet. Catal. Lett.* **2000**, 70, 67-72.

(63)   Janiak, T.; Okal, J., *Appl. Catal. B: Environ.* **2009**, 92, 384-392.

(64)   Krishnankutty, N.; Vannice, M. A., *J. Catal.* **1995**, 155, 312-326.

(65)   Matyi, R. J.; Schwartz, L. H.; Butt, J. B., *Catal. Rev.-Sci. Eng.* **1987**, 29, 41-99.

(66)   Canton, P.; Fagherazzi, G.; Battagliarin, M.; Menegazzo, F.; Pinna, F.; Pernicone, N., *Langmuir* **2002**, 18, 6530-6535.

(67)   Pinna, F.; Menegazzo, F.; Signoretto, M.; Canton, P.; Fagherazzi, G.; Pernicone, N., *Appl. Catal. A: Gen.* **2001**, 219, 195-200.

(68)   Hadjiivanov, K. I.; Vayssilov, G. N., *Adv. Catal.* **2002**, 47, 307-511.

(69)   Sales, E. A.; Jove, J.; Mendes, M. de Jesus; Bozon-Verduraz, F., *J. Catal.* **2000**, 195, 88-95.

(70)   Guerrero-Ruiz, A.; Yang, S.; Xin, Q.; Maroto-Valiente, A.; Benito-Gonzalez, M.; Rodriguez-Ramos, I., *Langmuir* **2000**, 16, 8100-8106.

(71)   Sheu, L.-L.; Karpinksi, Z.; Sachtler, W. M. H., *J. Phys. Chem.* **1989**, 93, 4890-4894.

(72)   Jujjuri, S.; Ding, E.; Shore, S. G.; Keane, M. A., *J. Mol. Catal. A: Chem.* **2007**, 272, 96-107.

(73)   Prelazzi, G.; Cerboni, M.; Leofanti, G., *J. Catal.* **1999**, 181, 73-79.

(74)   Conner, W. C.; Falconer, J. L., *Chem. Rev.* **1995**, 95, 759-788.

(75)   Adams, B. D.; Ostrom, C. K.; Chen, S.; Chen, A., *J. Phys. Chem. C* **2010**, 114, 19875-19882.

(76)   Hong, C.-T.; Yeh, C.-T.; Yu, F.-H., *Appl. Catal.* **1989**, 48, 385-396.

(77)   Liu, J., *ChemCatChem* **2011**, 3, 934-948.

(78)   Anderson, J. R.; Pratt, K. C. In *Introduction to Characterization and Testing of Catalysts,* Academic Press: Sydney, 1985; Vol. p 61.

(79)   Baer, D. R.; Gaspar, D. J.; Nachimuthu, P.; Techane, S. D.; Castner, D. G., *Anal. Bioanal. Chem.* **2010**, 396, 983-1002.

(80)   Briggs, D.; Seah, M. P.   In *Practical Surface Analysis by Auger and X-ray Photo-electron Spectroscopy,* first ed.; Wiley: Chichester, 1983; Vol. 1, p 26.

(81)   Hub, S.; Hilaire, L.; Touroude, R., *Appl. Catal.* **1988**, 36, 307-322.

(82)   Jiang, L.; Gu, H.; Xu, X.; Yan, X., *J. Mol. Catal. A: Chem.* **2009**, 310, 144-149.

(83)   Ramos, A. L. D.; Alves, P. D. S.; Aranda, D. A. G.; Schmal, M., *Appl. Catal. A: Gen.* **2004**, 277, 71-81.

(84)   Gómez-Sainero, L. M.; Seoane, X. L.; Fierro, J. L. G.; Arcoya, A., *J. Catal.* **2002**, 209, 279-288.

(85)   Larichev, Y. V.; Moroz, B. L.; Bukhtiyarov, V. I., *Appl. Surf. Sci.* **2011**, 258, 1541-1550.

(86)   Tribolet, P.; Kiwi-Minsker, L., *Catal. Today* **2005**, 105, 337-343.

(87)   Semagina, N.; Renken, A.; Kiwi-Minsker, L., *J. Phys. Chem. C* **2007**, 111, 13933-13937.

(88)   Crespo-Quesada, M.; Yarulin, A.; Jin, M. S.; Xia, Y. N.; Kiwi-Minsker, L., *J. Am. Chem. Soc.* **2011**, 133, 12787-12794.

(89)   Coq, B.; Tijani, A.; Figuéras, F., *J. Mol. Catal.* **1991**, 68, 331-345.

(90)   Crespo-Quesada, M.; Andanson, J. M.; Yarulin, A.; Lim, B.; Xia, Y. N.; Kiwi-Minsker, L., *Langmuir* **2011**, 27, 7909-7916.

(91)   Zina, M. S.; Ghorbel, A. (2004) Pd-Mo Bimetallic Catalysts Supported on Y-Zeolite: Effect of Molybdenum on Structural and Catalytic Properties of Palladium in Partial Hydrogenation of 1,3 butadiene in *Recents Advances in the Science and Technology of Zeolites and Related Materials* (van Steen, E.; Claeys, M.; Callanan, L. H., Eds.), pp 2364-2370, Elsevier, Cape Town.

(92)   Amorim, C.; Wang, X.; Keane, M. A., *Chin. J. Catal.* **2011**, 32, 746-755.

(93)   Zhao, B.; Chen, Y. W., *J. Non-Cryst. Solids* **2010**, 356, 839-847.

(94)   Li, H.; Zhao, Q.; Li, H., *J. Mol. Catal. A: Chem.* **2008**, 285, 29-35.

(95)   Tu, W.; Cao, S.; Yang, L.; Wang, W., *Chem. Eng. J.* **2008**, 143, 244-248.

(96)   Liu, H.; Liang, M.; Xiao, C.; Zheng, N.; Feng, X.; Liu, Y.; Xie, J.; Wang, Y., *J. Mol. Catal. A: Chem.* **2009**, 308, 79-86.

(97)   Yoneda, T.; Takido, T.; Konuma, K., *J. Mol. Catal. A: Chem.* **2007**, 265, 80-89.

(98)   Lee, I.; Morales, R.; Albiter, M. A.; Zaera, F., *Proc. Natl. Acad. Sci. U. S. A.* **2008**, 105, 15241-15246.

Table 1: Catalyst source or preparation method (for laboratory synthesised samples), Pd loading, BET surface area and hydrogenation performance in terms of product selectivities at a common fractional p-CNB conversion ($X_{p\text{-}CNB} = 0.2$).

Catalyst	Catalyst Source/ Peparation	Pd loading (% w/w)	BET area ($m^2 \ g^{-1}$)	$S_{X_{p\text{-}CNB} = 0.2}$ (%)		
				p-CAN	AN	NB
Pd[a]	Commercial	-	2	29	55	16
Pd/AC-I[b]	Prepared by impregnation	5.5	875	74	0	26
Pd/AC-II	Commercial	10.2	826	38	52	10
Pd/SiO$_2$[b]	Prepared by impregnation	7.7	178	0	90	10
Pd/Al$_2$O$_3$-I[b]	Prepared by deposition	0.9	157	0	78	22
Pd/Al$_2$O$_3$-II	Commercial	1.2	160	0	38	62
Pd/Al$_2$O$_3$-III[b]	Prepared by impregnation	6.9	173	0	68	32
Pd/ZnO[b]	Prepared by deposition	4.7	8	100	0	0

[a]generated by reduction of PdO; [b]laboratory synthesised

Table 2. Temperature and H/Pd ratio associated with Pd hydride decomposition and Pd nanoparticle size obtained from TEM (d_{TEM}), CO (d_{CO}) and H_2 (d_{H_2}) chemisorption.

Catalyst	Pd hydride		Pd nanoparticle size		
	T (K)	H/Pd (mol mol^{-1})	d_{TEM} (nm)	d_{CO} (nm)	d_{H_2} (nm)
Pd	377	0.67	-	-	-
Pd/AC-I	365	0.29	11.7	8.2	129.0
Pd/AC-II	373	0.16	4.4	19.9	4.7
Pd/SiO$_2$	362	0.36	12.6	36.7	9.4
Pd/Al$_2$O$_3$-I	343	0.25	6.4	28.8	4.1
Pd/Al$_2$O$_3$-II	355	0.05	2.4	2.3	2.0
Pd/Al$_2$O$_3$-III	377	0.33	9.6	49.0	25.0
Pd/ZnO	356	0.22	6.5	14.6	4.0

Figure Captions

Figure 1: Temperature-programmed reduction (TPR) profiles for **(I)** bulk PdO, **(II)** Pd/AC-II **(III)** Pd/Al$_2$O$_3$-II and **(IV)** Pd/ZnO.

Figure 2: Representative TEM images and Pd nanoparticle size distributions for **(I)** Pd/AC-II (with standard deviation of the mean (σ_m) as a function of the number of Pd particles counted (n)), **(II)** Pd/Al$_2$O$_3$-II and **(III)** Pd/ZnO.

Figure 3: Relationship between Pd nanoparticle size (d_{TEM}) and **(I)** H$_2$ chemisorption (open symbols; dashed line) and **(II)** *p*-CNB transformation rate (solid symbols; solid line); Pd supported on AC (□, ■), *non*-reducible oxides (○,●) and ZnO (Pd/ZnO: △,▲; Pd/ZnO-PVP; ★,☆).

Figure 4: XPS spectrum over the Pd 3*d* region for Pd/ZnO: XPS experimental data are represented by symbols (□) while the lines are the result of spectra curve fitting with independent contributions due to Pd^0 (dashed line) and PdZn alloy (dotted line) from peak deconvolution.

Figure 5: Relationship between binding energy (BE) of the Pd 3$d_{5/2}$ signal and Pd nanoparticle size (d_{TEM}) for Pd supported on activated carbon (□), *non*-reducible oxides (○) and ZnO (△). *Note*: shaded area illustrates the BE region that is characteristic of Pd^0 (80).

Figure 6: Selectivity (S_i) to *p*-CAN (●), AN (○) and NB (△) as a function of *p*-CNB fractional conversion ($X_{p\text{-}CNB}$) for reaction over **(I)** bulk Pd **(II)** Pd/AC-II **(III)** Pd/Al$_2$O$_3$-II and **(IV)** Pd/ZnO.
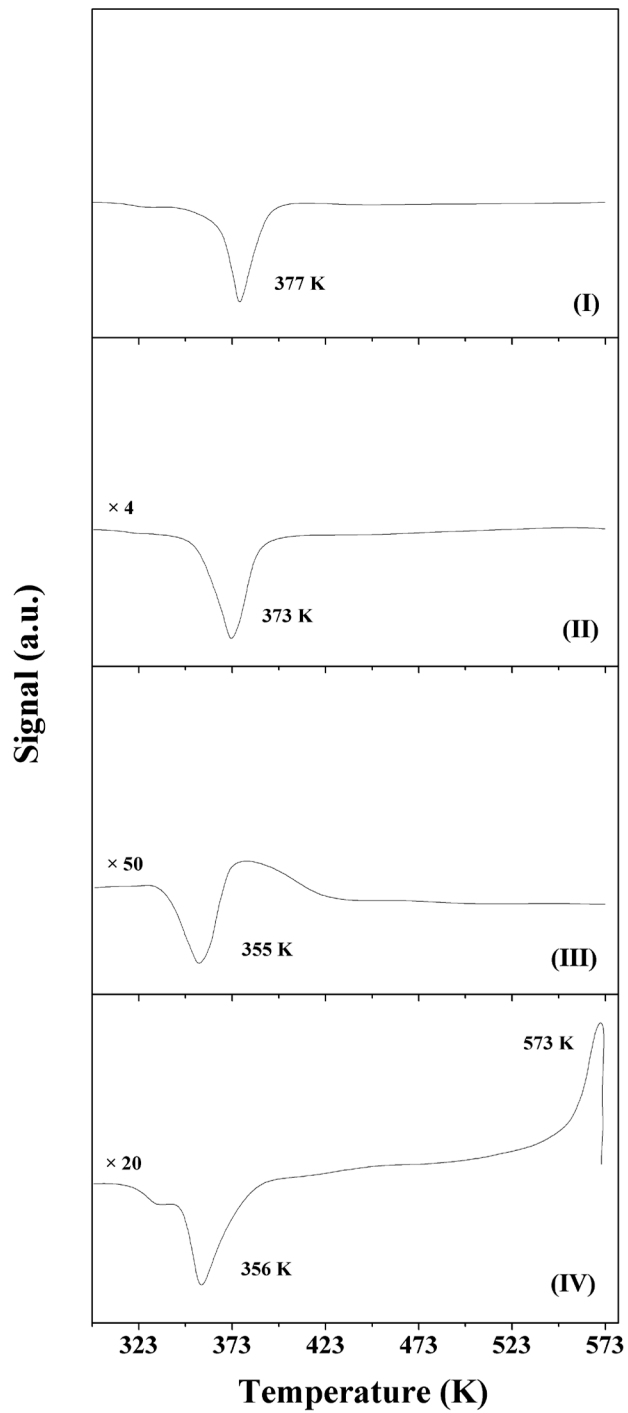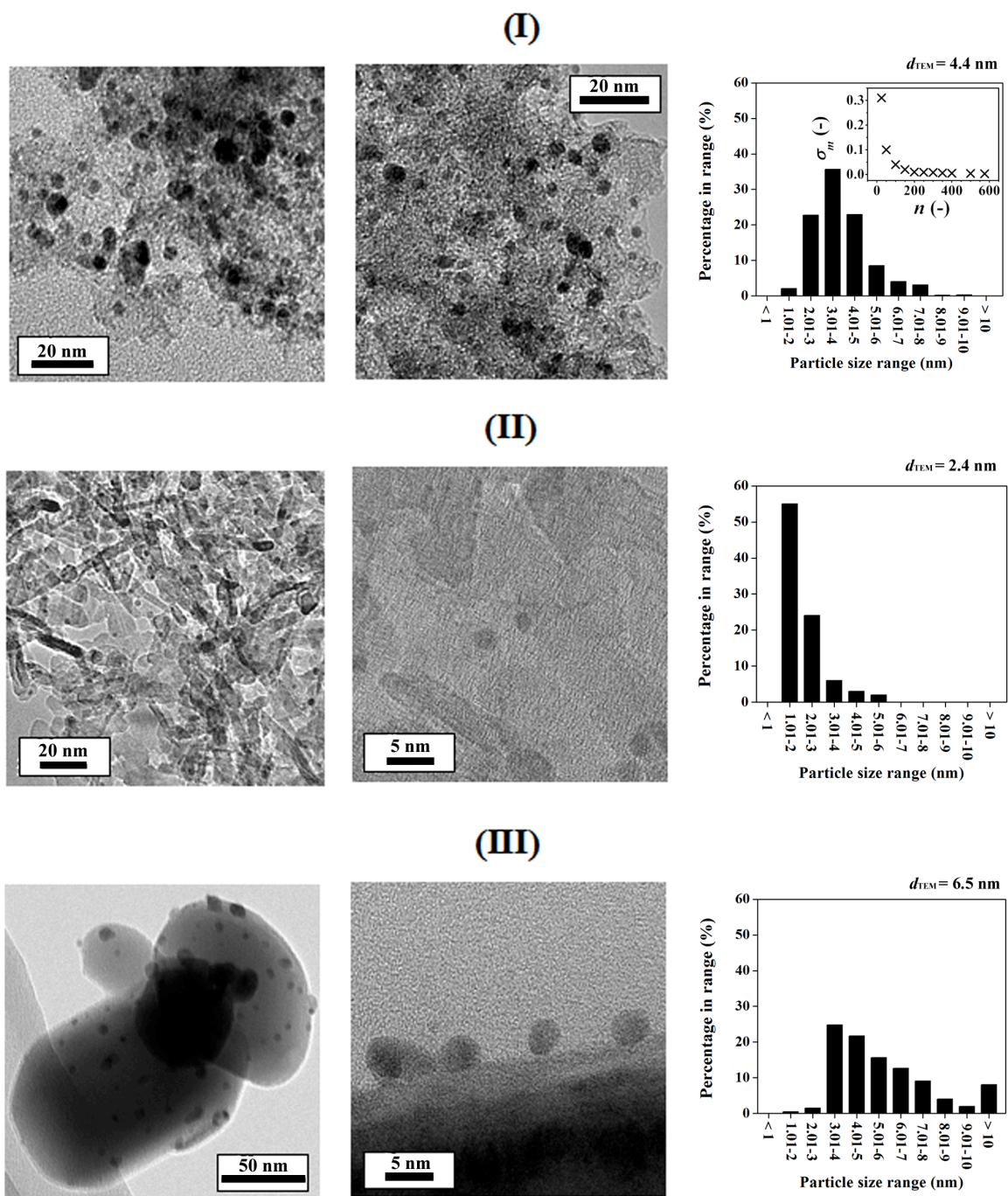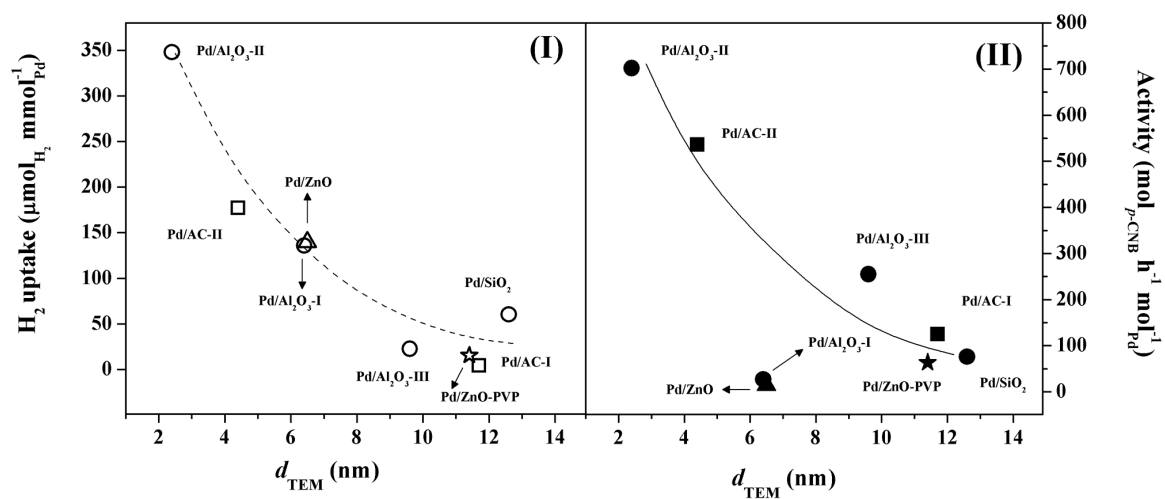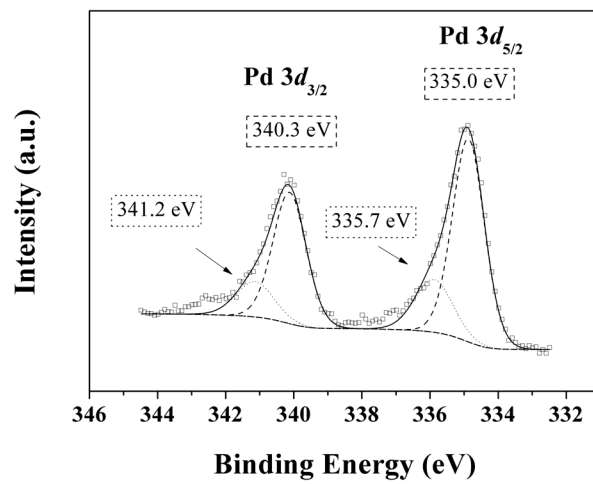
Figure 1

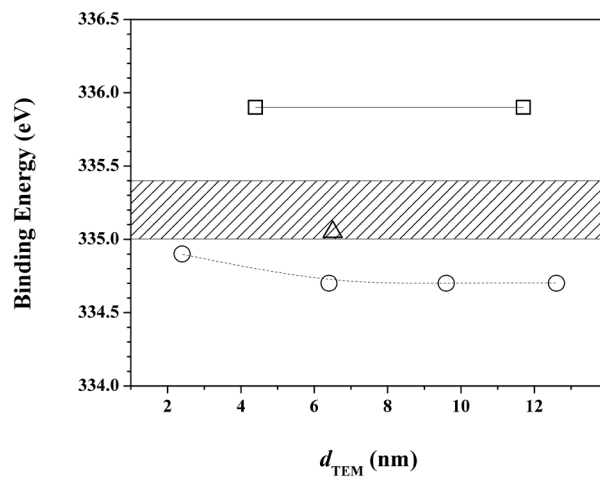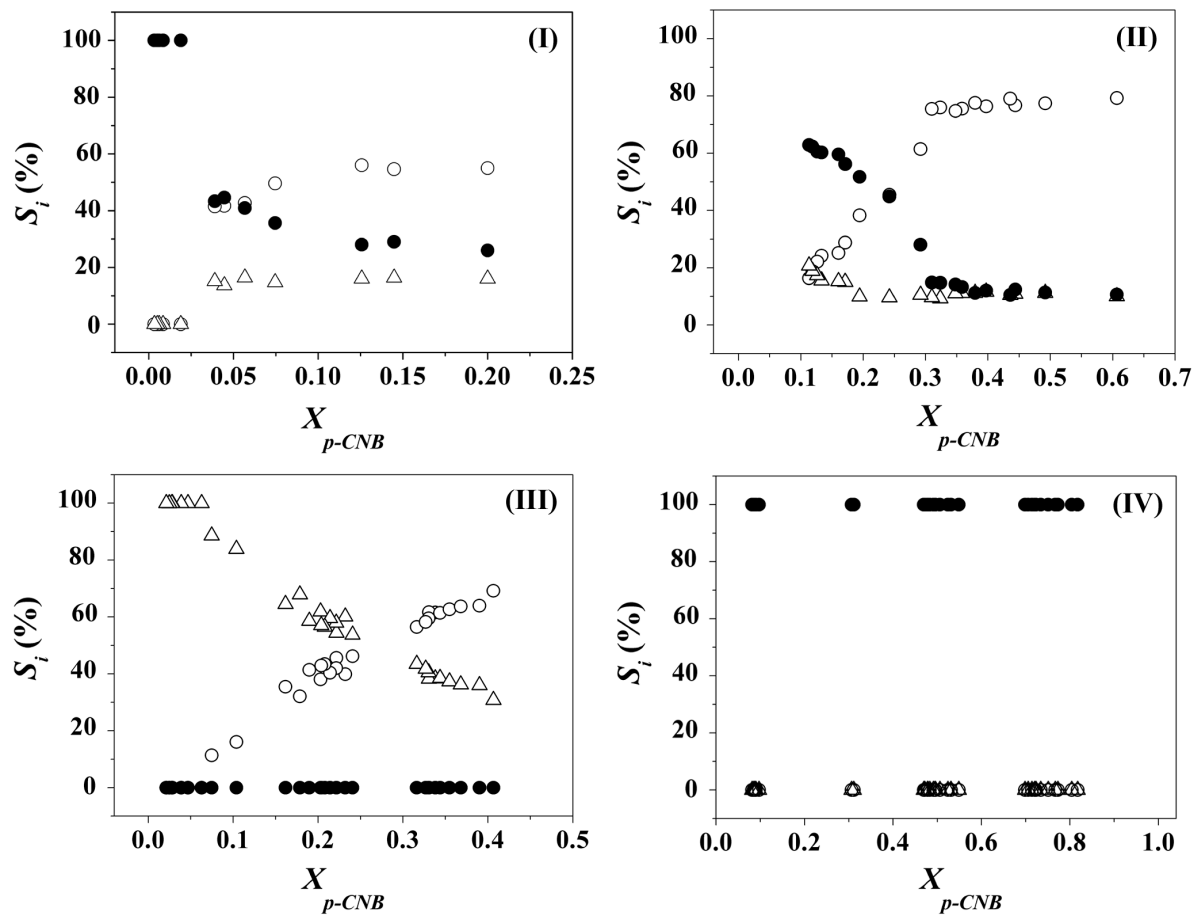**Figure 2**

(I)

(II)

(III)

Figure 3

Figure 4

Figure 5

Figure 6

Scheme 1: Reaction scheme for the hydrogenation of *p*-chloronitrobenzene (*p*-CNB). The targeted route **(I)** to *p*-chloroaniline (*p*-CAN) is given by the open arrow.

Scheme 1